Study by electron microscopy of proton exchange membrane fuel cell membrane-electrode assembly degradation mechanisms: Influence of local conditions

Laure Guétaz*, Sylvie Escribano, Olivier Sicardy

CEA, LITEN, DEHT-LCPEM, 17 rue des Martyrs, 38054 Grenoble, France

ABSTRACT

Observations of microstructural evolution by scanning and transmission electron microscopy in different regions of aged membrane/electrode assemblies (MEA) have shown that degradation is not always uniform through the MEA surface; after load cycling operation, the degradation is more severe in the region located near the air inlet compared to air outlet. After constant load operation the degradation appears more uniform. Two types of microstructural evolution have been observed. The first one consists in the modification of the cathode leading to nanoparticles larger than initially but still well dispersed. The second type of evolution ends up with big agglomerates formed by large Pt particles in the cathode, with also a noticeable degradation of the carbon support, both phenomena being always coupled with the precipitation of Pt particles inside the membrane. The first type of evolution results from the electrochemical Ostwald ripening mechanism and appears when the cathode potential remains low. In contrast, the second one appears when the cathode is locally exposed to a high interfacial potential resulting from the reverse-current mechanism. Hydrogen starvation induced by the load cycles and oxygen crossover that increases with membrane damage, are the two main factors responsible for this severe degradation mechanism.

© 2012 Elsevier B.V. All rights reserved.

1. Introduction

The proton exchange membrane fuel cells (PEMFC) cost and lifetime remain the two major technical barriers for their acceptance as a practical power source. These two points are often interrelated, for example minimizing the amount of Pt catalyst or decreasing the polymer membrane thickness tends to decrease the PEMFC lifetime. Thus, in order to optimize both the cost and lifetime, it is essential to better understand the different degradation mechanisms. During operation, PEMFC exhibit a gradual decline in power output. Their performance decay rate strongly depends on the operating conditions (current or voltage load, stationary or cycling load, temperature, gas humidity …) [1,2]. The irreversible decline in performance is caused by the degradation of the different materials constituting the fuel cell. Different fuel cell components are affected [2–4]. Examples include the chemical/physical degradation of Teflon used in the gas diffusion layer (GDL) leading to GDL hydrophobicity loss; chemical/physical degradation of the membrane that modifies its two main properties, high proton conductivity and low gas permeability; carbon support corrosion and platinum nanoparticle dissolution and sintering that decrease the electrochemical active surface. The degradation mechanisms of each material are particularly difficult to completely understand because they are not only affected by many external factors (depending on operating conditions) but they can also be interrelated (for example, carbon corrosion can be enhanced by increasing O_2 permeability of the membrane and furthermore carbon corrosion can strongly modify the Pt nanoparticle distribution). Moreover, the degradation of the different materials is often not uniform; differences can be observed through the electrode thickness [5] or between different zones of the electrode surface (for example in the gas inlet or outlet regions …) [6,7]. Hence, if we want to determine the relative contribution of each component's degradation to the performance degradation of the entire fuel cell, it is essential to better understand the degradation mechanisms of materials in the different zones of the electrodes.

In this study the microstructure evolution of membrane-electrode assemblies (MEA) aged under different conditions — a constant load mode and a load cycling mode — have been

carefully analyzed by scanning electron microscopy (SEM) and transmission electron microscopy (TEM). The microstructure degradation has been studied in two particular selected regions; the first one is located near the air inlet and the second one near the air outlet. Two types of MEA microstructural evolution have been observed and each of them has been associated to one specific degradation mechanism.

2. Experimental

2.1. MEA preparation

Catalyst coated backings (CCB) MEA type have been used. Gas diffusion electrodes (GDE) were prepared by coating the catalyst ink onto gas diffusion layers (GDL). The ink consisted of Solvay Solexis Aquivion™ dispersion (ref. D83-06A) and 46 wt% Pt/C Vulcan catalyst supplied by Tanaka Kikinzoku Group (ref. TEC10V50E). The GDL was the grade 25BC of SGL-Group. The cathode and anode Pt loadings were of about 0.4 and 0.25 mg$_{Pt}$ cm^{-2} respectively. The two electrodes were assembled with a 30 μm thick Solvay Solexis Aquivion™ membrane (EW 790 g eq.$^{-1}$) (ref. E79-03S) in order to obtain a MEA with a geometric active surface area of 25 cm^2.

2.2. Durability testing

MEA were tested using a 25 cm^2 counter-flow single cell, operating at 80 °C with hydrogen and air fed in counter-flow. Two condition modes were used: a constant load mode at fixed current density of 0.6 A cm^{-2} and a load cycling mode. In the latter mode, the current density varied between 0.12 A cm^{-2} and 0.6 A cm^{-2} with the frequency of one cycle per minute as described in Fig. 1(a). Gas flow rates were controlled by applying a fixed stoichiometric ratio of 1.5 for hydrogen and 2 for air, with an absolute gas pressure of 1.5 bar and a relative humidity of 40% for hydrogen and 60% for air.

In the study it was decided to stop the ageing tests after a few hundreds of hours or after failure if this occurred before 500 h of testing. So, the aged MEA considered in this study have been aged during approximately 600 h for the stationary test case and only 450 h for the load cycling-mode case that has been stopped due to membrane failure. These two tests can be considered as reference cases for two extreme situations, with on one hand smooth constant operation stopped before failure and on the other hand more aggressive cycling operation conducted until failure.

2.3. SEM and TEM analysis

The MEA microstructures of the fresh and aged MEA were analyzed by scanning electron microscopy (SEM) and transmission electron microscopy (TEM). For both aged MEA, the microstructure degradation was studied in two surface regions; the first one located near the air inlet and the second one near the air outlet (Fig. 1(b)), corresponding respectively to the hydrogen outlet and to the hydrogen inlet since ageing tests were performed in counter-flow operation.

For SEM and TEM investigations, small pieces (15 × 8 mm^2) were taken from the MEA in the selected regions and then embedded in epoxy resin. Cross-section samples (8 mm long, cut perpendicularly to the gas channel) were first prepared by mechanical polishing until mirror-like surface were obtained and then observed by SEM. Afterwards the 1 mm long region of interest was chosen from these embedded samples to prepare thin sections that were cut using a LEICA ultramicrotome and then investigated by TEM. SEM and TEM observations were respectively performed using a ZEISS LEO 1500 field emission gun (FEG) − microscope and a JEOL 2000FX conventional TEM microscope.

2.4. X-ray diffraction measurements

The crystalline structure of Pt nanoparticles was characterized by X-ray diffraction in Bragg-Brentano geometry on a Bruker D8 Advance diffractometer using Cu-Kα X-ray source. The average size of the crystallites was determined using the Scherrer law:

$$D = \frac{K\lambda}{\beta \cos(\theta)}$$

where D is the crystallite size, K the so-called Scherrer constant ($K = 0.89$ in case of spherical shape), λ the X-ray wavelength (here $\lambda = 0.15406$ nm), β the full-width at half maximum of the considered diffraction peak and θ its Bragg angle. The instrumental contribution to the peaks broadening was measured in order to correct the β values and enter in the formula only the grain size contribution. Measurements were performed using the (220) reflection of face-centred cubic Pt as this X-ray line exhibits sufficient intensity and does not overlap with the other lines of the diagram. The same regions as in TEM and SEM analysis were investigated. For each sample, the two electrodes were dissociated in order to investigate separately the anode and the cathode. Because of the low Cu-Kα radiation absorption in the carbon support and ionomer and the low Pt content, the penetration
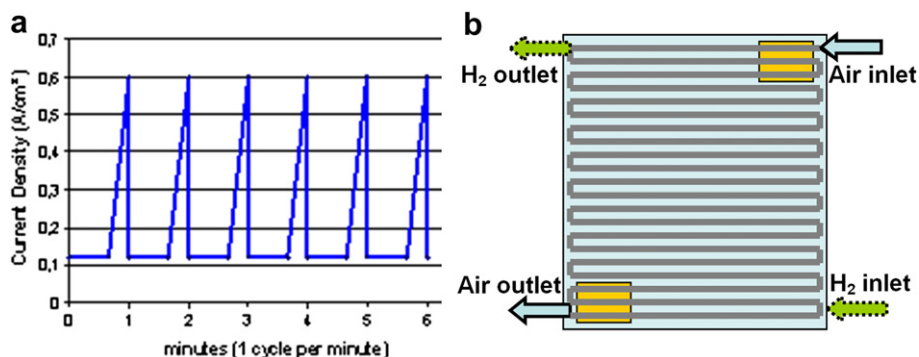

Fig. 1. Experimental conditions. (a) Current density load profile applied versus time for the ageing test in load cycling mode. (b) Schematic localization versus the active surface of the single cell and MEA of the samples selected from the aged MEA for SEM and TEM investigations.

depth of the X-ray beam is greater than the active layer thickness : in these conditions, the collected Pt diffracted signal is representative of the totality of Pt present in the electrode whatever its in-depth localization. The analyzed areas range over few mm^2 and the accuracy of the crystallite size measurements is about ±0.1 nm.

3. Results

3.1. MEA life testing

Fig. 2(a) and (c) shows the ageing test results with the cell voltage evolution respectively for constant load and load cycling operations. Fig. 2(b) and (d) shows the polarization curve evolution during the two ageing tests (time of the measurements is indicated by arrows on the voltage versus time graphs).

During stationary operation, there is a degradation of the electrode performances with an increase of the activation and diffusion over-potentials during time. However, the test has been stopped and restarted after 500 h showing that an important part of this performance degradation is reversible. This voltage recovery after restart is attributed to water profile stabilization during the stop, with probably an evacuation of the excess of water out of the cathode active layer or redistribution within the MEA. During cycling with the same type of MEA, the performances are decreasing more or less in the same way during 350 h but then the voltage degradation slope increases dramatically due to the membrane degradation which increases rapidly before failure, showing the main problem caused by operation under these cycling

conditions. So in the cycling case it has not been possible to check the reversibility of the performance loss after a stop and restart.

3.2. Fresh MEA microstructure

SEM image of the fresh MEA cross-section (Fig. 3(a)) show the structure of the MEA without the GDL. The active layers are around 7 μm thick at the cathode side (upper electrode) and 4 μm thick at the anode side (lower electrode). The fresh MEA catalyst layer microstructure was observed by TEM on a thin cross-section sample (Figs. 3(b) and 4(a)). The carbon support structure and porosity can be observed on low magnification images (Fig. 3(b)) whereas higher magnification images (Fig. 4(a)) show well-dispersed Pt nanoparticles on the carbon support. The Pt nanoparticle size measured on TEM images appears around 3 nm which is consistent with the average nanoparticle size measured by XRD (Fig. 5).

3.3. Microstructure degradation of the MEA aged under load cycling operation

3.3.1. MEA located near the air inlet

SEM observations of the MEA cross-section show that, after load cycling ageing test (stopped after MEA failure), the degradation of the MEA is particularly severe in the zone located near the air inlet (Fig. 6(a)). In some zones (zone A in Fig. 6(a)), the MEA is dramatically degraded: the membrane becomes thinner until holes are formed and the cohesion between the membrane and the electrodes disappears. In other zones, like Zone B (in Fig. 6(a)), the membrane appears less damaged although the cathode
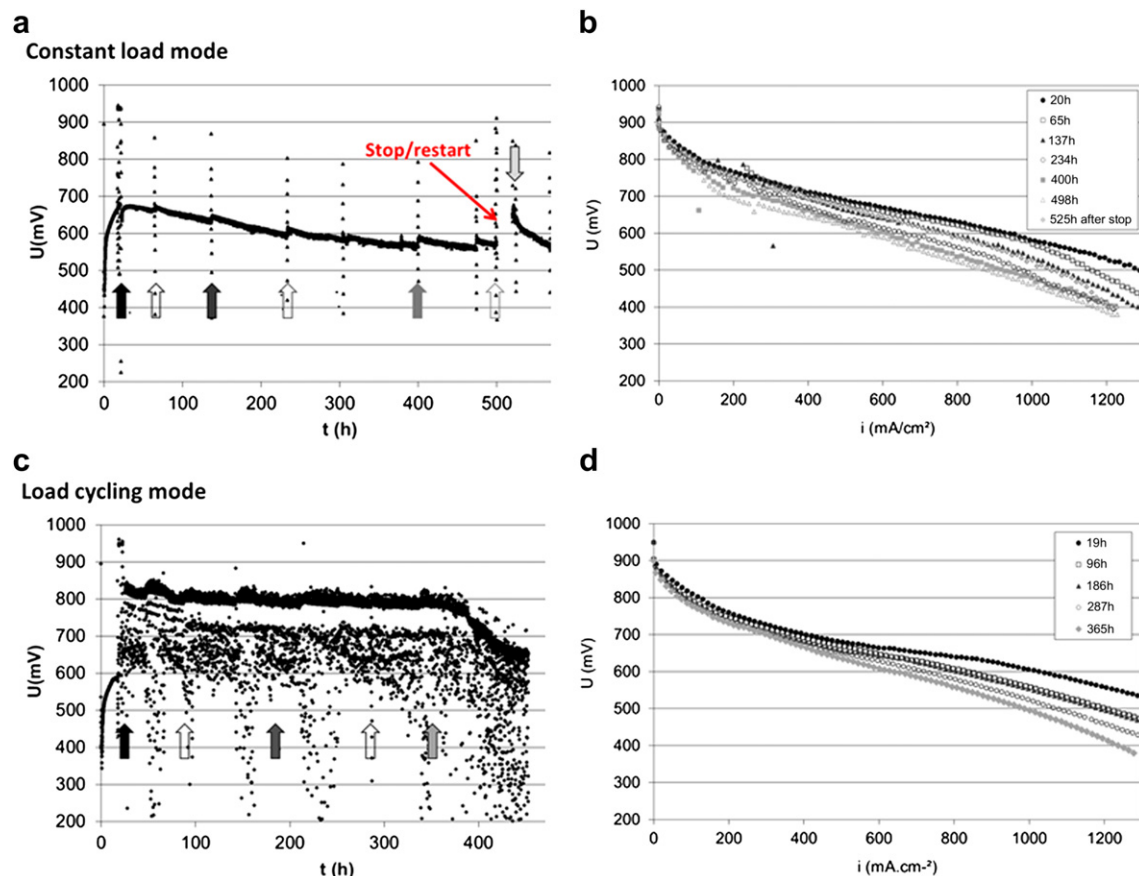

Fig. 2. MEA ageing test data. (a) and (c) show the cell voltage versus time respectively for constant load operation at 0.6 A cm^{-2} and load cycling mode between 0.12 and 0.6 A cm^{-2}. (b) and (d) show the polarization curves measured at different time of these two tests (the time when a polarization curve is measured is indicated by arrows on (a) and (c)).
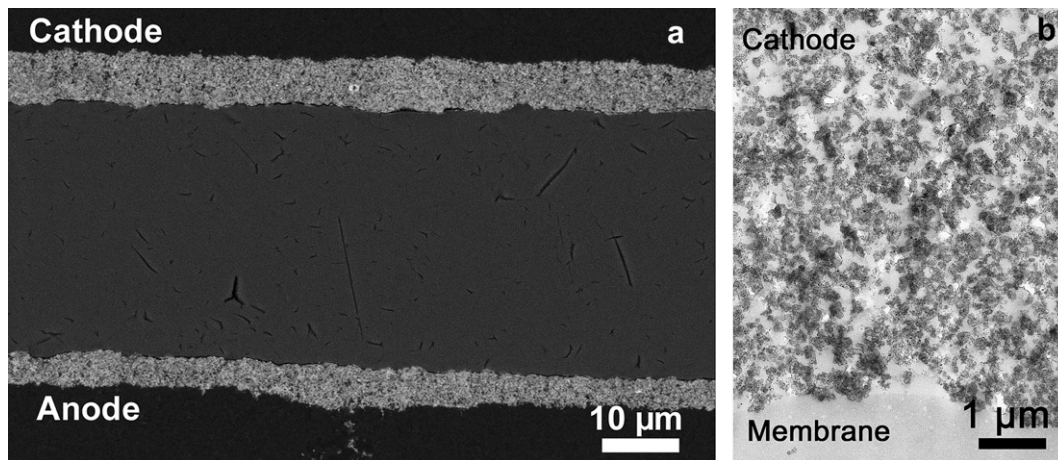
Fig. 3. a) SEM image of the fresh MEA cross-section. (b) Low magnification TEM image of the thin fresh MEA cross-section showing the carbon support microstructure and the porosity within the active layer.

microstructure is degraded. In addition, all along the cross-section, the images show a large amount of Pt precipitates inside the membrane (that appear as bright dots, indicated by arrows in Fig. 6(b) and (c)). In order to better characterize the active layer degradation, an MEA cross-section thin sample has been observed by TEM, with the sample being taken in zone B. The cathode microstructure was first observed. Low magnification TEM cathode images (Fig. 7(a)) show that the carbon structure is modified with the presence of large holes that were not observed in the fresh MEA (Fig. 3(b)). Higher magnification TEM images (Fig. 4(b)) show that the catalyst nanoparticle size has dramatically increased. XRD measurements (Fig. 5) indicate an average Pt particle size of 13 nm that is in agreement with the particle size measured on the TEM images. The nanoparticles are no more uniformly distributed inside the cathode but they form large agglomerates (Fig. 7(b)). Moreover,

an important particle accumulation is observed in the cathode active layer near the GDL side as indicated in Fig. 7(a).

As shown the SEM images (Fig. 6(b) and (c)), platinum has precipitated inside the membrane and has formed a band of nanoparticles centred at 6 μm from the cathode/membrane interface. TEM cross-section observations reveal that the larger particles located at the centre of the band have a diameter around 100 nm (Fig. 8(a)). No particles have been observed in the first 4 μm of the membrane near the cathode/membrane interface whereas smaller particles have been observed from the centre of the band until the anode/membrane interface. The platinum precipitation continues towards the anode/membrane interface where a larger amount of particles (darker band) is observed (Fig. 8(b)). Fig. 4(c) shows the Pt nanoparticle distribution inside the anode. The nanoparticle size increases throughout the anode;
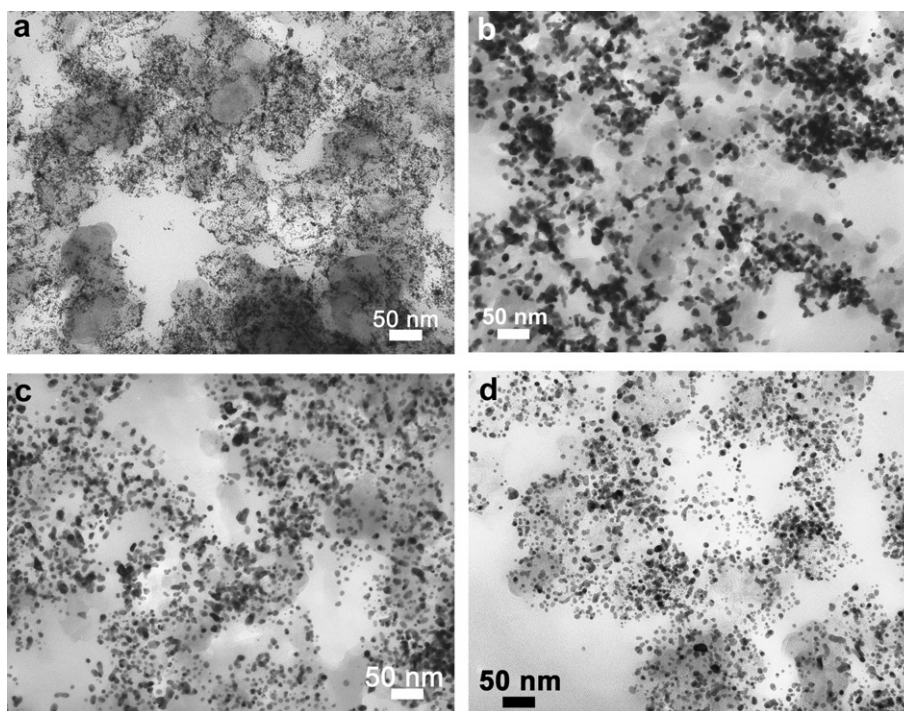

Fig. 4. TEM images of nanoparticle distribution in (a) the fresh MEA, (b) in the cathode after ageing under load cycling operation, in the air inlet zone, (c) in the anode of the same zone and (d) in the cathode in the air outlet zone.
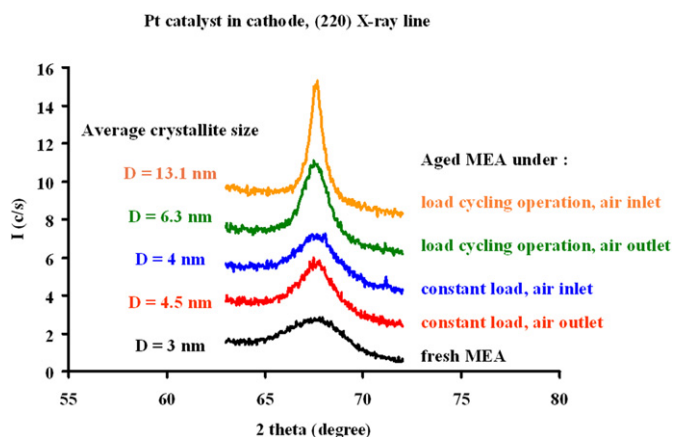
Fig. 5. X-Ray diffraction line of the (220) reflection of Pt recorded for the different cathodes analyzed by TEM; fresh one and after ageing in constant load operation and under load cycling operation. For aged cathodes, the analyses were performed in the air inlet and air outlet zones. For each sample, the average sizes of the crystallites are reported in the figure.

XRD measurements indicate an average particle size of 6.6 nm. The nanoparticles remain well distributed inside the anode; no large agglomerates are observed, except at the anode/membrane interface.

3.3.2. MEA located near the air outlet

SEM images of the cross-section of MEA located near the air outlet show that in this region the MEA degradation is less important (Fig. 9). Although some separation between the active layer and the membrane is observed in some zones, like in zone A on Fig. 9, no important membrane damage such as thinning or piercing has been observed. The degradation of the cathode is also less important as compared to the air inlet zone. The structure of the carbon support, observed on the low magnification TEM images, appears similar to the fresh MEA (Fig. 3(b)). The cathode degradation mainly consists in Pt nanoparticles coarsening until an average size of 6.3 nm as measured by XRD (Fig. 5). Unlike in the

cathode located near the air inlet zone, the catalysts remain well dispersed without forming important particle agglomerates (Fig. 4(d)). No platinum precipitation has been observed inside the membrane or at the anode/membrane interface. At the anode side, only a small Pt particle size increase has been observed, XRD measurement indicates an average particle size of 4.4 nm.

3.4. Microstructure degradation of MEA aged under constant load operation: MEA located near the air inlet and near the air outlet

The degradation of the MEA aged under constant current operation at 0.6 A cm^{-2} appears similar in the two zones located near the air inlet and near the air outlet. The degradation is comparable to the degradation observed in the MEA aged under load cycling operation and located near the air outlet (see Section 3.3.2). No severe membrane damage along the MEA cross-section has been observed by SEM and neither carbon structure damage nor platinum precipitation inside the membrane or at the anode/membrane interface have been observed by TEM. The main cathode microstructure evolution is the Pt nanoparticle coarsening until an average diameter measured by XRD (Fig. 5) around respectively 4 and 4.5 nm in the air inlet region (Fig. 10(a)) and air outlet region (Fig. 10(b)). In these two regions, the nanoparticles remain well dispersed, without large aggregate formation. In the anode side, only small Pt particle coarsening is observed and an average particle size of 4.2 and 4 nm are measured by XRD in the air inlet and air outlet regions respectively.

4. Discussion

Analysis of the microstructure evolution in different regions of the MEA surface clearly shows that the degradation of the MEA is not always uniform across the surface. It appears that, in the ageing modes chosen in this study, when the MEA is aged under load cycling operation, the degradation is more important in the MEA region located near the air inlet (H$_2$ outlet) than in the region located near the air outlet (H$_2$ inlet). On the other hand, when the MEA is aged under constant load operation, the degradation appears more uniform.
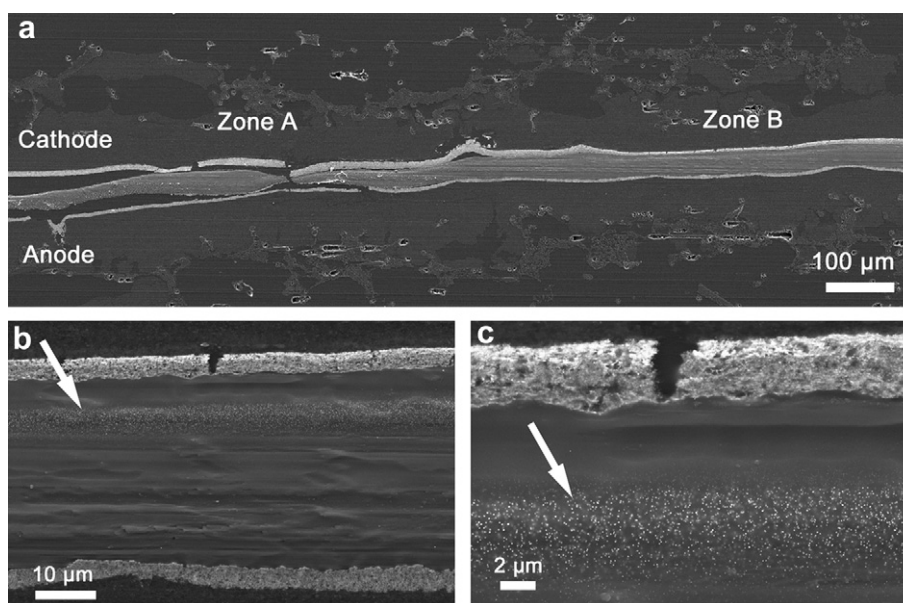

Fig. 6. SEM images of a MEA after ageing under load cycling operation: cross-section located in the air inlet zone. (a) In some zones, like zone A, MEA is dramatically degraded; with membrane thinning and holes and no more cohesion between the membrane and the electrodes. In other zones, like zone B, the membrane appears less damaged. (b) and (c) larger magnification of (a) showing modified cathode microstructure and a large amount of Pt particles inside the membrane (indicated by the arrow).
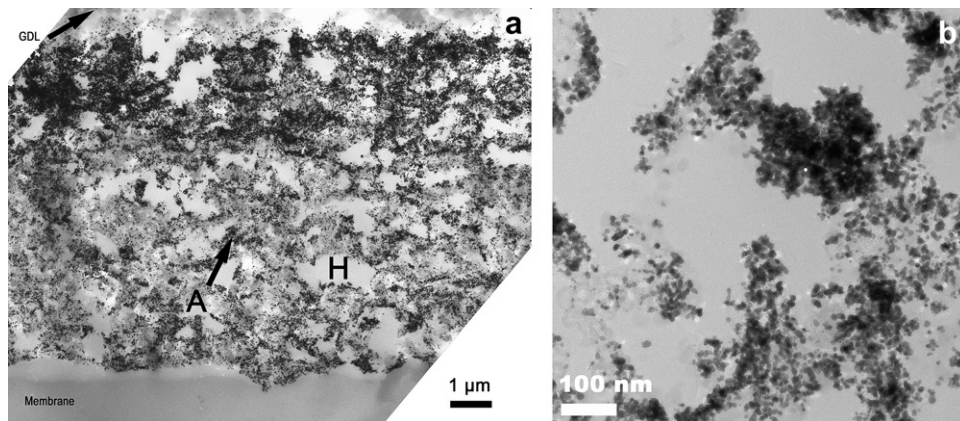
Fig. 7. TEM images of a MEA after ageing under load cycling operation: thin cross-section of the cathode active layer located in the air inlet zone. (a) Low magnification image showing on one hand that the carbon structure is modified with the appearance of large holes (*indicated by H*) and on the other hand that the Pt nanoparticles form large agglomerates (*indicated by A*). An important particle accumulation is also observed at GDL side. (b) Higher magnification images showing the large Pt nanoparticle agglomerates.

By analyzing the Pt nanoparticle distribution across the aged MEA, it appears that there are two types of MEA microstructural evolution. The features of the first one consist of nanoparticles increased in size at the cathode with generally a mean diameter much smaller than 10 nm. In this case, the nanoparticles remain well dispersed on the carbon support and no particles are observed inside the membrane nor at the anode/membrane interface and no carbon support degradation is detected. This first type of microstructural evolution has been observed for the MEA aged under load cycling operation in the zone located near the air outlet and for the MEA aged under constant load in the two zones located near the air inlet and outlet. On the other hand, the feature of the second type of MEA microstructural evolution consists of large particles (in this study larger than 10 nm) that are no more uniformly dispersed inside the cathode but that form large agglomerates associated with the observation of the carbon support degradation and the precipitation of Pt particles inside the membrane or/and at the anode/membrane interface. This second type of microstructural evolution has been observed for the MEA aged under load cycling operation in the zone located near the air inlet. These two different MEA microstructural evolutions suggest that two different degradation mechanisms are involved in the MEA degradation, depending on the local conditions.

The first mechanism that leads to the first type of microstructural evolution consisting in well-dispersed particles increased in size is assumed to be the electrochemical Ostwald ripening mechanism whereas the mechanism that leads to the second type of microstructural evolution consisting in the agglomeration of large particles is the reverse-current mechanism. These two mechanisms are described below in order to confirm that they can lead to the observed final microstructures.

4.1. Electrochemical Ostwald ripening mechanism

The Ostwald ripening mechanism is probably the main mechanism of MEA degradation under the majority of operation conditions. It occurs by the growth of the larger particles at the expense of smaller ones which dissolve. This mechanism was widely studied in metallic alloys as a second phase coarsening process [8,9]. The growth originates from atomic diffusion induced by concentration gradients around the particles. This gradient is caused by the fact that in equilibrium the concentration at the surface of larger particles is lower than that of smaller particles, which is described by the well known Gibbs–Thomson relation.

From an analogical point of view, the coarsening process in electrochemical system is considered to be driven by the particle
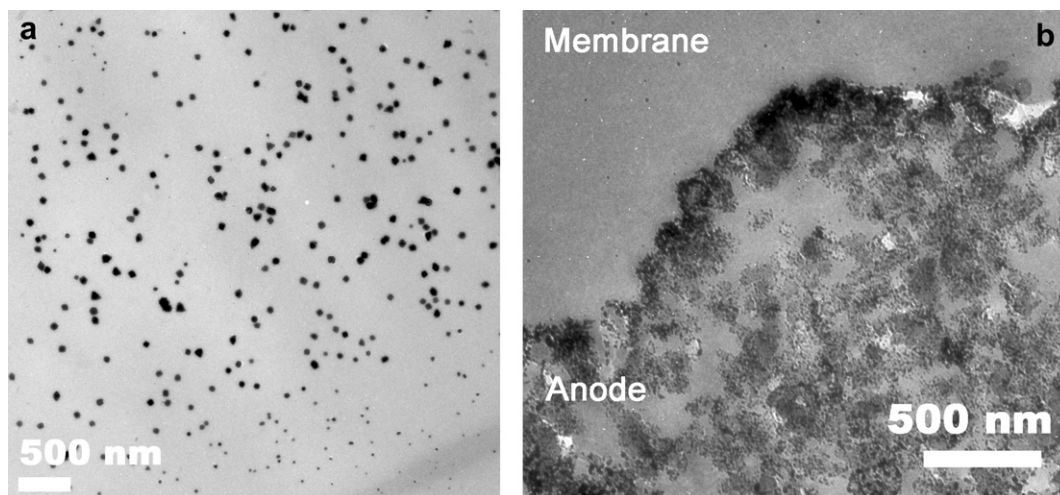

Fig. 8. TEM images of (a) the membrane in the air inlet zone after ageing under load cycling operation showing the largest particles (with a diameter around 100 nm) located at the centre of the band, (b) the anode/membrane interface located in the same zone showing a platinum enrichment at the interface (darker band).
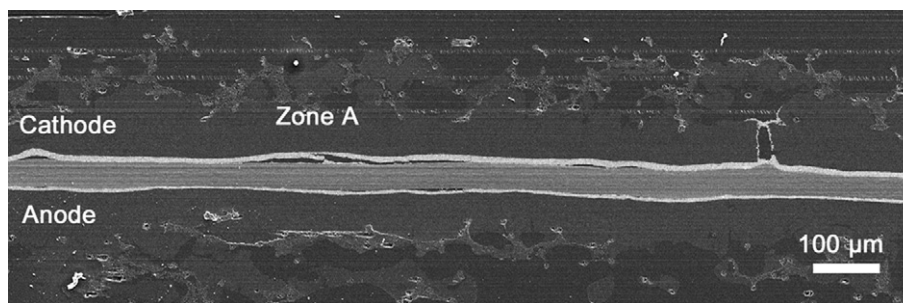
Fig. 9. SEM images of a MEA after ageing under load cycling operation: cross-section located in the air outlet zone. No important membrane damage such as thinning or piercing has been observed. However, in some zones as shown in the zone A, decohesion between the active layer and the membrane has been observed.

size dependence of the standard electrode potential of the material. This dependence also results from the Gibbs–Thomson relation. According to Plieth [10], the standard electrode potential of nanoparticles E^0_{particle} is negatively shifted with respect to the bulk metal E^0_{bulk} electrode potential and this shift is proportional to the reciprocal radius of the particle $1/r$ following the equation:

$$\Delta V = E^0_{\text{particle}} - E^0_{\text{bulk}} = -\frac{2\gamma V_{\text{m}}}{zF}\frac{1}{r} \tag{1}$$

where γ is the surface tension, V_{m} is the molar volume, F is the Faraday's constant and z the number of charges involved in the electrochemical reactions. Fig. 11 shows a plot of the shift in the standard electrode potential of Pt nanoparticles as a function of radius, where the Pt surface tension is 3.3 J m^{-2} according to Plieth [10]. The negative shift is particularly important for particles smaller than 5 nm.

In this electrochemical process, atomic transport from the smaller particles to the larger ones occurs by ionic species diffusing through the electrolyte and electron transfer through the conducting support is required to re-establish electrical equilibrium [11]. Therefore this mechanism appears between neighbouring particles that are electrically connected both by the support and by the electrolyte. As mentioned by Ferreira et al. [5], in this process the transport of the platinum species in the ionomer phase is at the nanometre scale. As a consequence, the particles increase in size but remain well dispersed on the carbon support. Moreover, this process does not involve the migration of the Pt species towards the membrane and generally occurs without leading to the formation of Pt nanoparticles inside the membrane. As shown in the TEM images (Fig. 4(d)), this mechanism usually produces larger monocrystalline nanoparticles with a spherical shape. Nevertheless some nanoparticle agglomerates can also be observed. These agglomerates have probably been formed in the zone where the density of nanoparticles was particularly high and where the enlargement of the nanoparticles has induced their coalescence.
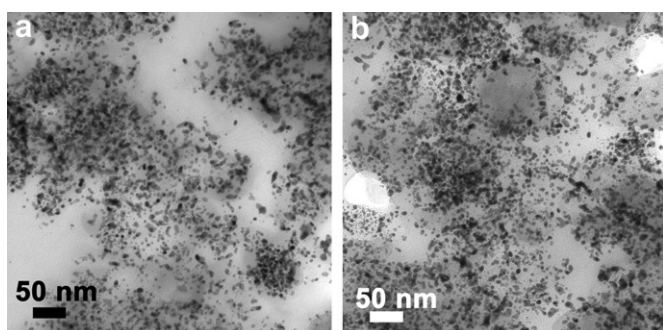
The main parameters that control this mechanism are the electrode potential, the electrical conductivity of the support and the ionic conductivity of the electrolyte [11]. Thus the nanoparticles will not grow in the region where no ionomer is present. For example growth will probably not occur for particles lying between carbon grains too close for allowing ionomer penetration and consequently a part of some initial particles of the active layer will probably remain small. Another example clearly showing that particles do not grow when no ionomer is present is illustrated on Fig. 12. This TEM image of the cathode active layer after ageing under constant load shows a micrometric zone (surrounded by a dashed line to guide the eye) that is not affected by the coarsening mechanism. In fact this zone is probably a micrometric defect of the active layer resulting from the Pt/C agglomeration (containing no ionomer) that has been formed during ink preparation.

On the other hand, as the ionic conductivity of the ionomer strongly depends on its water content, the particle growth will be more important in the MEA region containing more water. For example, we have observed in another study that after an ageing test under constant load, the particles were larger near the cathode/membrane interface where more water is produced than near the cathode/GDL interface.

The electrode potential is also an important parameter that controls the kinetics of the particle coarsening, a higher potential enhances the kinetics. However, this mechanism can probably occur already at low potential. As the Ostwald electrochemical ripening mechanism is observed in the MEA aged at constant load that operated under a mean potential around 0.6–0.7 V (Fig. 10), this suggests that the mechanism is already active around 0.6 V. This potential is coherent with the study of Tang et al. [12] who have directly observed the dissolution of small particle at 0.65 V using in-situ electrochemical scanning tunnelling microscopy.

Fig. 10. TEM images of the nanoparticle distributions in the cathode after ageing under constant load operation located (a) in the air inlet zone and (b) in the air outlet zone.
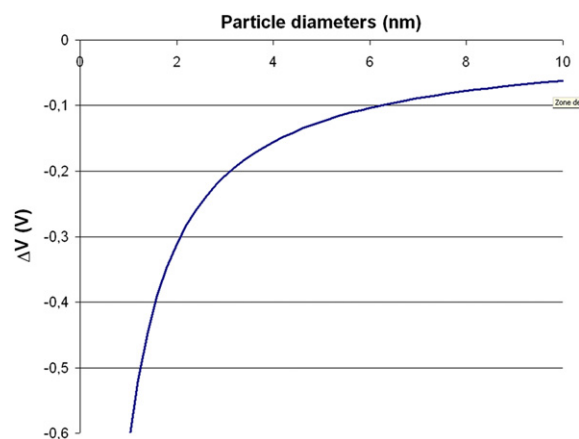

Fig. 11. Plot of the shift in the standard electrode potential of Pt nanoparticles as a function of radius, where the Pt surface tension is 3.3 J m^{-2} according to Plieth [10].
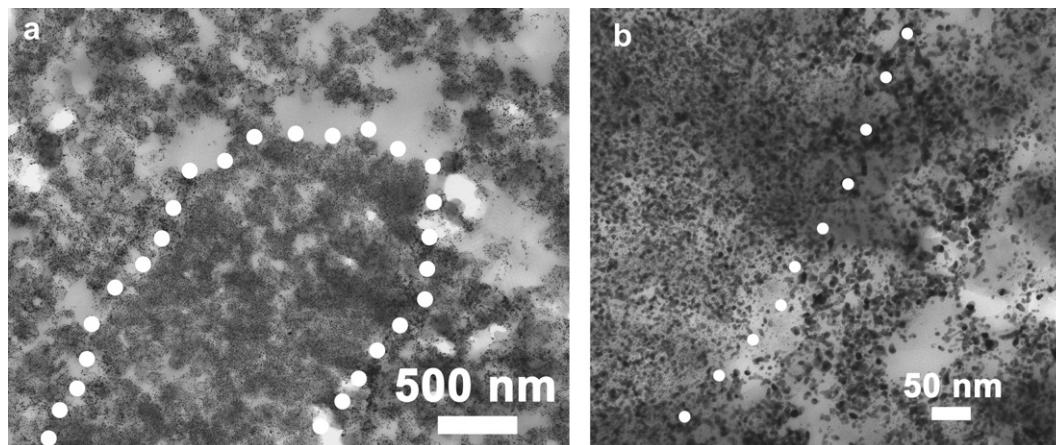
Fig. 12. a) TEM image showing a zone in the cathode active layer (in the air outlet region after ageing under constant load) where no particle growth has occurred. This zone probably corresponds to agglomerated Pt/C grains containing no ionomer that were formed during the ink preparation. (b) higher magnification showing the small particles at the left part and the larger one at the right part.

It is also important to note, that the kinetics of particle coarsening is faster when the particles are small because of a higher thermodynamic driving force. The kinetics of particle coarsening is given either by [13,9]:

$$d_t^2 - d_0^2 = K_S t \tag{2}$$

in the assumption of an interface-controlled mechanism or by:

$$d_t^3 - d_0^3 = K_D t \tag{3}$$

in the assumption of a mechanism controlled by the diffusion through the media. This last equation describes well the precipitate coarsening in metallic alloys for which a large number of models have been proposed [9]. In these two equations, d_0 and d_t are particle size respectively at the initial time and after time t. K_S and K_D are kinetic parameters (units $cm^2 s^{-1}$ or $cm^3 s^{-1}$) which are a function of the material, temperature and the electrolyte [13]. These two equations show that the particle coarsening is faster during the first hundred hours than after the following ones. This fact has been confirmed by many studies showing a greater loss of the electrochemical surface area during the first hundred hours of operation compared to the next ones [1,5,14]. Our analyses performed on differently aged MEA (for many other studies) suggest that the coarsening kinetic probably becomes much slower when the particles reach a kind of limit size. This limit seems to be around 10−15 nm, which is the larger particle size we have observed in many MEA aged under different conditions even after 20,000 h.

When considering all these specific characteristics, the electrochemical Ostwald ripening mechanism will lead to the following MEA microstructure evolution: i) well-dispersed monocrystalline spherical nanoparticles, with possibly a few agglomerates. The average particle diameter is generally smaller than 10 nm. ii) No particle growth where no electrolyte is present. iii) Larger coarsening where more water is present in the MEA. iv) No nanoparticle within the membrane.

As all these characteristics are in good agreement with the microstructural features observed in the MEA aged under constant load operation (in the air inlet and outlet zones) and under load cycling operation in the air outlet zone, this clearly confirms that in these 3 samples the electrochemical Ostwald ripening has been the main ageing mechanism. This mechanism probably appears at a potential as low as 0.6 V but when the local cathode potential becomes higher, probably at more than 0.9 V, other mechanisms described below appear.

4.2. Reverse-current mechanism

The second type of MEA microstructural evolution observed in the air inlet zone of the MEA aged under load cycling operation and consisting of large particle agglomerates associated with carbon support degradation and precipitation of Pt particles inside the membrane is suggested to be caused by the reverse-current decay mechanism. This mechanism has been proposed by Reiser et al. [15] to explain performance degradation assumed to occur when the anode is exposed to oxygen, the oxygen being introduced from outside or through the membrane. They explain that this situation can occur during a start-stop procedure when air is present on the anode due either to leakage from outside air or when there is a local hydrogen starvation on the anode due to a bad hydrogen supply or when the oxygen crossover through the membrane is too important.

These abnormal cell conditions result in a high interfacial potential difference (between the electrode conductive materials and the electrolyte) in the region where oxygen is present on the anode side and create an overpotential on the cathode enabling carbon corrosion.

This reverse-current mechanism is well described by Reiser et al. [15] or Takeuchi et al. [16]. Reiser et al. [15] have developed a simplified one-dimensional mathematical model to obtain the potential profiles inside the MEA during reverse-current conditions. Takeuchi et al. [16] have proposed a two dimensional model. The results obtained by Reiser et al. [15] are considered here for analyzing the microstructural degradation we have observed in our sample. In their model, they consider a MEA divided in two sections, region A and region B (upper part of the Fig. 13). In region A, the anode side was assumed to be exposed to H_2 and the cathode side to air, while in region B both electrodes are exposed to air. For the anode reactions, an H_2 oxidation reaction is considered for region A while an oxygen reduction reaction is accounted for in region B. For cathode reactions, O_2 evolution and reduction and carbon oxidation reactions are accounted for in region B. Due to the high electron conductivity of the GDL, the authors assumed that the anode metal potential V_m^a and the cathode metal potential V_m^c are maintained along the electrode respectively to 0.0 V and 0.85 V. In these conditions, the authors have calculated the electrolyte potential ϕ along the electrodes (Fig. 13) and they show that available O_2 and associated ORR in the anode of region B lowers ϕ to $\phi = -0.59$ V, leading to maintain the interfacial potential difference of the anode electrode $(V_m^a - \phi)$ closer to $V_{O_2}^{eq}$ $(V_m^a - \phi = 0.59$ V).

Consequently, the interfacial potential difference of the cathode ($V_m^c - \phi$) becomes higher ($V_m^c - \phi = 1.4$ V). This high difference in potential allows oxidation reactions not allowed in the normal situation and can result in oxygen evolution and carbon corrosion. Hence, as carbon oxidation occurs in the MEA cathode whereas oxygen reduction occurs in the MEA anode, in the region B, protons migrate from the cathode to the anode (a phenomenon referred to as "the reverse-current" mechanism).

In the present study, TEM analysis of the MEA microstructural evolution suggest that the reverse-current mechanism has appeared in the zone located near the air inlet of the MEA aged under load cycling operation. Indeed, as partial hydrogen starvation can appear in this air inlet zone during operation, the local situation can have met the conditions required for the occurrence of this mechanism. As the ageing tests are conducted using counter flow, the H_2 outlet zone is in front of the air inlet zone. Partial hydrogen starvation can result from a bad gas supply during the cycling; since gas flows are controlled with fixed stoichiometry (1.5 stoichiometric ratio for H_2), it is possible that during short transition periods when current is increased from minimum to maximum, there is a delay in providing needed hydrogen and not enough hydrogen is available in this H_2 outlet zone. In our case, the cycles are not supposed to allow air at the anode side from the outside (no stops). Anode flooding that could appear in this region [17] will also enhance hydrogen starvation. Moreover, at the air inlet zone, oxygen crossover can occur, first at low level due to natural permeation, but also at a higher level if the membrane is physically damaged. In fact, in this air inlet zone, significant degradation of the membrane is definitely observed with zones where the membrane is clearly pierced at the end of the test (Fig. 6). These local conditions, i.e. possible hydrogen starvation and important oxygen crossover, clearly correspond to the situation able to produce the reverse-current mechanism previously described.

The membrane failure in this air inlet zone is not surprising because in this zone the humidity of the membrane is low as the air relative humidity is only 60% and low membrane humidity promotes its degradation [18,19]. Moreover, due to the counter-flow gas supply and the cycling mode, the membrane is subject to large hydration variation during the cycling that also induces significant membrane degradation [20].

As described above (Fig. 13), the presence of oxygen in a part of the anode enhances the interfacial potential difference in cathode and then accelerates the carbon corrosion that damages the cathode structure. In addition, this high interfacial potential difference can enhance platinum oxidation and lead to significant Pt nanoparticle dissolution, followed by an important modification of the Pt distribution inside the MEA. The carbon corrosion is most often considered as the main consequence of the reverse-current mechanism. This fact can be explained because when important carbon corrosion occurs, the electrode structure is completely destroyed and this results in a fatal fuel cell performance decay [7]. However, carbon corrosion, when it is not too severe, is hardly detectable by TEM observations contrary to the change of Pt distribution. In this study, it appeared therefore interesting to consider the Pt distribution evolution inside the MEA for a deeper analysis of the degradation mechanism. Under high potential [21] and particularly under cycling potential [22,23], Pt nanoparticle dissolution gives rise to a large amount of Pt charged species that can migrate over a long distance in the electrolyte. These Pt species can migrate towards the membrane and then be reduced by the hydrogen crossover to form particles in the membrane [5,24,25]. The Pt species can also migrate inside the cathode where they can be reduced during the low potential period of the potential cycle [5]. This redeposition process probably gives rise to the formation of particle agglomerates inside the cathode. In fact, the redeposition probably occurs in some favourable sites, like Pt nanoparticles surrounded by electrolyte, leading to large polycrystalline agglomerates similar to those obtained using a Pt electrodeposition process [26]. The Pt nanoparticle distribution is also directly affected by the carbon corrosion. When the corrosion of carbon is severe some Pt nanoparticles can be detached from the carbon support and rearranged within the active layer. When the particles remain attached to the carbon support, neighbouring particles can approach due to the carbon surface shrinkage, leading again to agglomeration [27]. Hence, the two degradation mechanisms (massive Pt nanoparticle oxidation/dissolution/redeposition and carbon corrosion) induced by the reverse-current mechanism lead to the formation of large particle agglomerates. It can be noticed that the dissolution/redeposition mechanism differs from the electrochemical Ostwald ripening mechanism as it implies no interaction between particles of different sizes. In the case of the dissolution/redeposition mechanism, the transport of the Pt species in the ionomer can occur on a larger scale (over many micrometres). As mentioned by Ferreira [5], the presence of Pt particles in the membrane provides unambiguous evidence for the migration of soluble Pt species in the ionomer on the micrometre scale. Hence
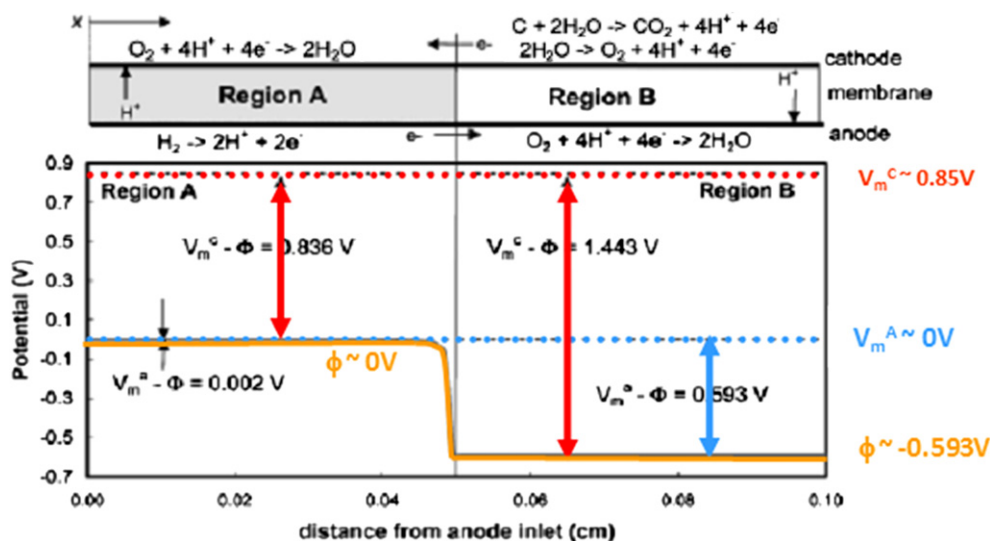

Fig. 13. Potential distribution along the MEA during reverse-current conditions. Reproduced by permission of the Electrochemical Society from Ref. [15].

the presence of particles in the membrane indicates that during the ageing test, the dissolution/redeposition mechanism has occurred and consequently that locally the cathode interfacial potential has been high enough to allow nanoparticle dissolution. Dynamic load profile is also an important factor that enhances platinum dissolution.

Moreover, let's consider the anode side in this air inlet zone. The model developed by Reiser et al. [15] shows a high interfacial potential difference at the anode side in the order of 0.6 V (Fig. 13). This potential can explain the particle growth observed in this H_2 outlet zone (Fig. 4(c)). In this case, the potential being similar to the potential of a cathode operating under normal condition, the electrochemical Ostwald ripening mechanism is probably the main mechanism leading to particles coarsening. The well-dispersed monocrystalline spherical Pt nanoparticles observed by TEM confirm the occurrence of this mechanism at the anode side.

Therefore, the MEA microstructural evolution (particles in the membrane, large agglomerates in the cathode, carbon corrosion, and well-dispersed spherical nanoparticles in the anode) observed in the air inlet/H_2 outlet zone of the MEA aged under load cycling operation is in very good agreement with the occurrence of the reverse-current mechanism. Then the MEA microstructural evolution analysis clearly evidenced that during the ageing test the anode side was exposed to oxygen. This results probably from a poor hydrogen supply during the cycling test but even more from the membrane degradation in this zone that has lead to significant oxygen crossover. More robust membranes such as reinforced membranes should limit the MEA degradation in this region.

5. Conclusions

SEM and TEM analyses of the microstructure evolution in different regions of the MEA surface have clearly shown that the degradation of the MEA is not always uniform across the surface. Particularly, when the MEA is aged under load cycling operation, the degradation is more severe in the MEA region located near the air inlet (hydrogen outlet). For the MEA aged under constant load mode, the degradation appears identical in the two regions (air inlet and outlet). In these different regions, two types of MEA microstructural evolutions have been observed. The first one, observed in the two analyzed regions (air inlet and air outlet) of the MEA aged under constant load mode and in the air outlet region in the MEA aged under load cycling mode, consists of a well-dispersed monocrystalline spherical nanoparticles in the cathode and no particle formation in the membrane. This microstructural evolution is characteristic of the electrochemical Ostwald ripening mechanism and probably appears when the cathode potential remains at the level of the mean potential of the cell (0.6–0.9 V).

The second type of MEA microstructural evolution, observed for the MEA aged under load cycling operation in the zone located near the air inlet, consists in large particle agglomerates and carbon degradation within the cathode active layer, in addition to platinum precipitation inside the membrane. This microstructural evolution results from exposition of the cathode to a high interfacial potential. This high interfacial potential which appears locally is explained by the reverse-current mechanism and is caused by the presence of oxygen at the anode. Hydrogen starvation that can be induced by the current cycles and significant oxygen crossover, that increases when the membrane is damaged, are two factors at the origin of this important catalyst degradation mechanism.

Finally, this work shows that observations of the local microstructural evolution in aged MEA can indicate if the electrodes have been locally exposed or not to a high interfacial potential.

References

[1] R.L. Borup, J.R. Davey, F.H. Garzon, D.L. Wood, M.A. Inbody, J. Power Sources 163 (2006) 76–81.
[2] F.A. de Bruijn, V.A.T. Dam, G.J.M. Janssen, Fuel Cells 8 (1) (2008) 3–22.
[3] R. Borup, J. Meyers, B. Pivovar, Y.S. Kim, R. Mukundan, N. Garland, D. Myers, M. Wilson, F. Garzon, D. Wood, P. Zenelay, K. More, K. Stroh, T. Zawodzinski, J. Boncella, J.E. McGrath, M. Inaba, K. Miyatake, M. Hori, K. Ota, Z. Ogumi, S. Miyata, A. Nishikata, Z. Simora, Y. Uchimoto, K. Yasuda, K. Kimijima, N. Iwashita, Chem. Rev. 107 (2007) 3904–3951.
[4] S. Zhang, X.-Z. Yuan, J.N.C. Hin, H. Wang, K.A. Friedrich, M. Schulze, J. Power Sources 194 (2009) 588–600.
[5] P.J. Ferreira, G.J. la O', Y. Shao-Horn, D. Morgan, R. Makharia, S. Kocha, H.A. Gasteiger, J. Electrochem. Soc. 152 (11) (2005) A2256–A2271.
[6] F. Ettingshausen, J. Kleemann, M. Michel, M. Quintus, H. Fuess, C. Roth, J. Power Sources 194 (2009) 899–907.
[7] F. Ettingshausen, J. Kleemann, A. Marcu, G. Toth, H. Fuess, C. Roth, Fuel Cells 11 (2) (2011) 238–245.
[8] I.M. Lifshitz, V.V. Slyozov, J. Phys. Chem. Solids 19 (1–2) (1961) 35–50.
[9] A. Baldan, J. Mater. Sci. 37 (2002) 2171–2202.
[10] W.J. Plieth, J. Phys. Chem. 86 (1982) 3166–3170.
[11] P.L. Redmond, A.J. Hallock, L.E. Brus, Nano Lett. 5 (1) (2005) 131–135.
[12] L. Tang, B. Han, K. Persson, C. Friesen, T. He, K. Sieradzki, G. Ceder, J. Am. Chem. Soc. 132 (2010) 596–600.
[13] V. Virkar, Y. Zhou, J. Electrochem. Soc. 154 (6) (2007) B540–547.
[14] J. Xie, D.L. Wood, K.L. More, P. Atanassov, R.L. Borup, J. Electrochem. Soc. 152 (5) (2005) A1011–A1020.
[15] C.A. Reiser, L. Bregoli, T.W. Patterson, J.S. Yi, J.D. Yang, M.L. Perry, T.D. Jarvi, Electrochem. Solid-State Lett. 8 (6) (2005) A273–A276.
[16] N. Takeuchi, T.F. Fuller, J. Electrochem. Soc. 155 (7) (2008) B770–B775.
[17] A. Morin, F. Xu, G. Gebel, O. Diat, Int. J. Hydrogen Energy 36 (2011) 3096–3109.
[18] J. Healy, C. Hayden, T. Xie, K. Olson, R. Waldo, M. Brundage, H. Gasteiger, J. Abbott, Fuel Cells 5 (2) (2005) 302–308.
[19] C. Chen, T.F. Fuller, Polym. Degrad. Stab. 94 (2009) 1436–1447.
[20] X.Y. Huang, R. Solasi, Y. Zou, M. Feshler, K. Reifsnider, D. Condit, S. Burlatsky, T. Madden, J. Polym. Sci. Part B Polym. Phys. 44 (2006) 2346–2357.
[21] X. Wang, R. Kumar, D.J. Myers, Electrochem. Solid-State Lett. 9 (5) (2006) A225–A227.
[22] K. Kinoshita, J.T. Lundquis, P. Stonehar, J. Electroanal. Chem. 48 (2) (1973) 157–166.
[23] Y. Shao, R. Kou, J. Wang, V.V. Viswanathan, J.H. Kwak, J. Liu, Y. Wang, Y. Lin, J. Power Sources 185 (2008) 280–286.
[24] T. Akita, A. Taniguchi, J. Maekawa, Z. Siroma, K. Tanaka, M. Kohyama, K. Yasuda, J. Power Sources 159 (2006) 461–467.
[25] E. Guilminot, A. Corcella, F. Charlot, F. Maillard, M. Chatenet, J. Electrochem. Soc. 154 (1) (2007) B96–B105.
[26] Z. Lin, L.W. Ji, X.W. Zhang, Matr. Lett. 63 (24–25) (2009) 2115–2118.
[27] Z.Y. Liu, J.L. Zhang, P.T. Yu, J.X. Zhang, R. Makharia, K.L. More, E.A. Stachc, J. Electrochem. Soc. 157 (6) (2010) B906–B913.